ELSEVIER

Effect of reactor heat transfer limitations on CO preferential oxidation

X. Ouyang, R.S. Besser*

Department of Chemical, Biomedical and Materials Engineering, New Jersey Center for Microchemical Systems, Stevens Institute of Technology, Castle Point on Hudson, Hoboken, NJ 07030, USA

Abstract

Our recent studies of CO preferential oxidation (PrOx) identified systematic differences between the characteristic curves of CO conversion for a microchannel reactor with thin-film wall catalyst and conventional mini packed-bed lab reactors (m-PBR's). Strong evidence has suggested that the reverse water-gas-shift (r-WGS) side reaction activated by temperature gradients in m-PBR's is the source of these differences. In the present work, a quasi-3D tubular non-isothermal reactor model based on the finite difference method was constructed to quantitatively study the effect of heat transport resistance on PrOx reaction behavior. First, the kinetic expressions for the three principal reactions involved were formed based on the combination of experimental data and literature reports and their parameters were evaluated with a non-linear regression method. Based on the resulting kinetic model and an energy balance derived for PrOx, the finite difference method was then adopted for the quasi-3D model. This model was then used to simulate both the microreactor and m-PBR's and to gain insights into their different conversion behavior.

Simulation showed that the temperature gradients in m-PBR's favor the reverse water-gas-shift (r-WGS) reaction, thus causing a much narrower range of permissible operating temperature compared to the microreactor. Accordingly, the extremely efficient heat removal of the microchannel/thin-film catalyst system eliminates temperature gradients and efficiently prevents the onset of the r-WGS reaction.
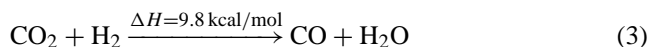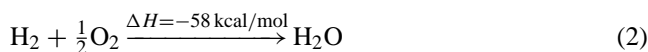© 2004 Elsevier B.V. All rights reserved.

Keywords: Preferential oxidation; Microreactor; Fuel processor; Heat transfer limitation; Non-isothermal reactor; Reverse water-gas-shift

1. Introduction

The deep removal of CO in a H_2-rich stream is a critical step in PEM fuel cell applications. In order to prevent poisoning of the fuel cell electrodes, the CO concentration needs to be reduced from ∼1% to below 10 ppm while conversion of H_2 is minimized. This step is referred to as CO preferential oxidation (PrOx) (Eqs. (1) and (2)). In our other work [1], we demonstrated that silicon microreactors coated with Pt/Al_2O_3 thin-film catalyst can effectively remove CO to below 10 ppm at 180 °C. In that study, discrepancies of the CO conversion temperature dependence were discovered

between the reaction results of the microreactors and those reported with conventional lab reactors in the literature:

$$CO + \tfrac{1}{2}O_2 \xrightarrow{\Delta H = -67 \text{ kcal/mol}} CO_2 \qquad (1)$$

$$H_2 + \tfrac{1}{2}O_2 \xrightarrow{\Delta H = -58 \text{ kcal/mol}} H_2O \qquad (2)$$

$$CO_2 + H_2 \xrightarrow{\Delta H = 9.8 \text{ kcal/mol}} CO + H_2O \qquad (3)$$

The studies based on conventional lab reactors with particulate catalyst found that there existed a narrow operating temperature window for acceptable CO conversion after light-off [2–4], followed by declining CO conversion as temperature was increased (Fig. 1). In contrast, our studies with microreactors showed essentially 100% CO conversion between 180

* Corresponding author. Tel.: +1 201 216 5257; fax: +1 240 255 4028.
  E-mail address: rbesser@stevens.edu (R.S. Besser).

Nomenclature

A_i	pre-exponential factor in kinetic expressions
Da	Damkőhler's number for heat transport
E_i	activation energy for kinetic expressions (J mol^{-1})
F_{tot}	total reactant flow $(\text{m}^3\,\text{s}^{-1}$ at 20 °C and 101,330 Pa)
ΔH_{ads}	adsorption energy (J mol^{-1})
k_i	specific reaction rate for r'_1, r'_2 and r'_3 $(i = 1, 2$ or 3)
$K_1,\ K_1^0$	adsorption equilibrium constant for CO
K_3	equilibrium constant of the r-WGS reaction
l	reactor axial position, $l = 0$ for the entrance of the reactor (m)
$l_{T_{max}}$	the axial position where the temperature (at $r = 0$) is the highest (m)
L	total reactor length (m)
P_i	partial pressure of reactant species i (i: CO, O_2, CO_2, H_2, H_2O) (Pa)
r	reactor radial position, $r = 0$ for the center of the reactor (m)
r'_1	reaction rate of CO in CO oxidation, moles of reactant per gram of active metal of catalyst per second $(\text{mol kg}^{-1}\,\text{s}^{-1})$
r'_2	reaction rate of H_2 in H_2 oxidation, moles of reactant per gram of active metal of catalyst per second $(\text{mol kg}^{-1}\,\text{s}^{-1})$
r'_3	reaction rate of CO_2 in r-WGS oxidation, moles of reactant per gram of active metal of catalyst per second $(\text{mol kg}^{-1}\,\text{s}^{-1})$
R	reactor radius (m)
S_{CO_2}	CO_2 selectivity (defined as the ratio of O_2 reacted with CO and total O_2 reacted)
t_{cat}	effective interparticle heat conduction distance: catalyst thickness for the microreactor or reactor inner radius for m-PBR (m)
T	local temperature in the reactor (°C)
$T_w,\ T_b$	reactor inner-wall temperature (°C)
WHSV	weight hourly space velocity, defined as mole of total reactant flow per mole of precious metal in the catalyst per hour (h^{-1})[1]
X_i	conversion of species i (i: CO, O_2, H_2)

Greek letter

β_i	reaction order for rate expression of H_2 oxidation (i: O_2, H_2, CO)

and 280 °C while there is only a slight drop-off (< 1%) at 300 °C, suggesting a much wider operating window for CO conversion (Fig. 1). An earlier explanation of this undesired

---
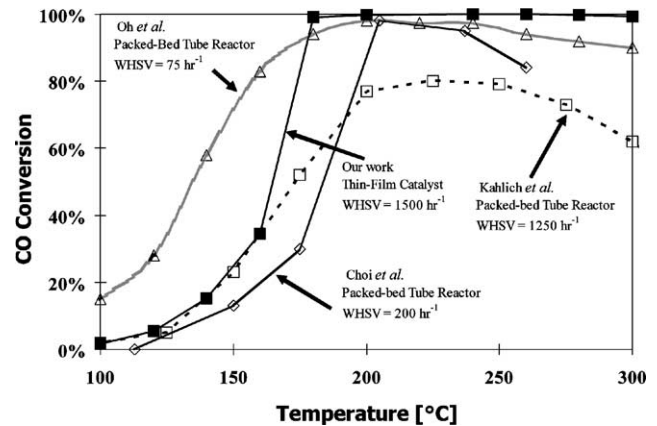
[1] Non-SI unit used by convention.

Fig. 1. CO conversion vs. temperature: comparison of the results of microreactor to results of other PrOx studies in the literature. WHSV: our work, 1500 h^{-1}; [2], 1250 h^{-1}; [3], 75 h^{-1}; [4], 200 h^{-1}.

CO conversion falloff at high temperatures was the competition between H_2 oxidation and CO oxidation [2]. Further investigations found that the falloff is caused by the heat transport limitations of conventional lab reactors [3–6]: the fast surface chemistry of the exothermic CO and H_2 oxidations leads to the accumulation of reaction heat in the catalyst bed; this situation then results in higher local temperatures (hot spots) and the favorable kinetics of the r-WGS reaction (Eq. (3)), which eventually limits the net CO conversion. 300 °C, suggesting a much wider operating window for CO conversion (Fig. 1). An earlier explanation of this undesired CO conversion falloff at high temperatures was the competition between H_2 oxidation and CO oxidation [2]. Further investigations found that the falloff is caused by the heat transport limitations of conventional lab reactors [3–6]: the fast surface chemistry of the exothermic CO and H_2 oxidations leads to the accumulation of reaction heat in the catalyst bed; this situation then results in higher local temperatures (hot spots) and the favorable kinetics of the r-WGS reaction (Eq. (3)), which eventually limits the net CO conversion.

Various researchers have shown an awareness of the importance of thermal management of PrOx reactors. Roberts et al. [6] studied the r-WGS reaction in PrOx with an adiabatic monolith reactor and found that full O_2 conversion in the adiabatic PrOx reactor caused the downstream temperature to increase to ~300 °C with an inlet temperature of only 170 °C, thus favoring the endothermic r-WGS reaction. Further, a 1D reactor model was developed by Choi et al. [4] to evaluate overall PrOx performance under various reactor heat exchange conditions (adiabatic, isothermal, etc.). They discovered that the net CO conversion drops significantly as the reactor operation changes from isothermal to adiabatic condition with the inlet gas temperature of 200 °C. However, both articles only considered heat transfer in the axial direction ignoring radial heat transfer resistance.

In our additional PrOx study, we discussed heat transfer limitations for both the microreactor and the mini packed-bed lab reactors (m-PBR's) based on Mear's criterion [1].

Due to the poor thermal conductivity of the porous catalyst materials, we concluded that significant thermal gradients could build up in both axial and radial directions even for the m-PBR's which are generally considered to possess low-radial transfer resistance due to their mm-scale diameters. Under the same reactor inner-wall (boundary) heat exchange conditions, the microreactor coated with thin-film wall catalyst removes reaction heat much more efficiently than the m-PBR's because of its extremely small catalyst thickness ($\sim 5 \times 10^{-6}$ m) and the resulting short radial heat conduction distance compared to that of the packed-bed catalyst used in m-PBR's (2×10^{-3} m). The comparatively longer heat conduction distances of the m-PBR's thus cause significant radial temperature gradients compared to the microreactor.

In order to quantitatively examine the impact of heat transport limitations on the PrOx reactor performance, we created a quasi-3D computational model for both the microreactor and m-PBR's. First, the reaction kinetic expressions based on the three major reactions involved in PrOx (Eqs. (1)–(3)) were formed and their parameters evaluated. Then a quasi-3D reactor model was built with the finite difference numerical method coupling both the mole and energy balance equations. Finally, results from the model are discussed to rationalize the difference of PrOx performance between the microreactor and m-PBR's.

2. Experimental

2.1. Microreactors, catalysts and parallel microreactor test bed

The kinetic data for PrOx was collected with the silicon microreactors used in our research [7]. The silicon chips used in this study were fabricated with well-known micromachining processes [8]. Photolithography and deep reactive ion etching (DRIE) by inductively coupled plasma (ICP) were the major techniques applied. Anodic bonding of the silicon chip to a piece of Pyrex® glass closed the reactor, before or after the catalyst incorporation in the microchannel. All reactors discussed in this paper have single channels with cross-sectional dimensions of 5×10^{-4} m (width) $\times 4.7 \times 10^{-4}$ m (depth) $\times 4.5 \times 10^{-2}$ m (length).

The Pt/Al$_2$O$_3$ catalyst with 2 wt.% platinum was synthesized using a sol–gel technique [9,10]. The catalyst precursor was then selectively deposited in the microchannel. Multiple layers were deposited by repeating the procedures followed by calcination. A 2×10^{-6} to 5×10^{-6} m catalyst thickness resulted in the catalyst weight of roughly 0.5×10^{-3} to 1.5×10^{-3} g.

A microkinetic array for fast catalyst screening and process studies developed in our lab was used for reaction tests. In this setup, four reactors are analyzed together with a gas sampling valve multiplexing between reactors. An online micro-GC (Varian 4900) and mass spectrometer (SRS QMS-200) are shared by the array for product analysis. Process control and data acquisition are automated with a LabVIEW program.

Details of the microreactor fabrication, thin-film catalyst synthesis and the microkinetic array are found elsewhere [1].

2.2. Kinetic rate expressions for reactions in PrOx

The majority of the reported PrOx kinetic studies has focused solely on the CO oxidation [11–13]. However, the incorporation of rate expressions of the coupled H$_2$ oxidation and r-WGS reactions is necessary for accurate representation of PrOx reaction behavior. Despite the importance of evaluation for all three reaction expressions, only few in the literature have addressed kinetic expressions for all three PrOx reactions [4]. Based on our previous work [1,14] and the PrOx kinetic studies in the literature [4], the kinetic expressions for PrOx reactions were formed as in the following equations:

$$r'_1 = \frac{k_1 P_{CO} P_{O_2}}{(1 + K_1 P_{CO})^2} \tag{4}$$

$$r'_2 = K_2 P_{O_2}^{\beta_1} P_{H_2}^{\beta_2} P_{CO}^{\beta_3} \tag{5}$$

$$r'_3 = k_3 \left(\frac{P_{CO_2} P_{H_2}}{K_3} - P_{CO} P_{H_2O} \right) \tag{6}$$

$$k_i = A_i \exp\left(-\frac{E_i}{RT}\right), \quad i = 1, 2, 3 \tag{7}$$

$$K_1 = K_1^0 \exp\left(\frac{\Delta H_{ads}}{RT}\right) \tag{8}$$

$$K_3 = \exp\left(\frac{4577.8}{T} - 4.33\right) \tag{9}$$

The majority of the PrOx studies used the power law expression for CO oxidation due to its simplicity [11–13]. This form is simplified from a Langmuir–Hinshelwood (L–H) expression and not suitable for small CO concentrations [5]. Therefore we adopted the full L–H expression instead of the power law expression for CO oxidation (Eq. (4)). The H$_2$ oxidation was previously modeled using empirical power law rate expressions by others [4]. However, in the presence of CO, the rate-limiting CO desorption strongly inhibits H$_2$ and O$_2$ adsorption and hence H$_2$ oxidation in PrOx [1]. Thus the incorporation of P_{CO} in the H$_2$ oxidation rate expression is necessary (Eq. (5)). The kinetics of r-WGS reaction was well studied previously [15], in which an empirical reversible rate expression [16] is attractive due to its relative simplicity and its appropriateness in PrOx kinetic studies as demonstrated previously [4]. With the rates of CO oxidation, H$_2$ oxidation and r-WGS reaction obtained, the net rates of individual reactant species (i.e., r'_{CO}, r'_{CO_2}, r'_{H_2}, r'_{H_2O}, r'_{O_2}) are calculated as in the following equations:

$$-r'_{CO} = r'_{CO_2} = r'_1 - r'_3 \tag{10}$$

$$-r'_{H_2} = r'_{H_2O} = r'_2 + r'_3 \tag{11}$$

$$-r'_{O_2} = 0.5(r'_1 + r'_2) \tag{12}$$

A multiple non-linear regression analysis with the Marquardt method [17] was selected to evaluate the independent variables $(A_1, A_2, A_3, E_1, E_2, E_3, \beta_1, \beta_2, \beta_3, K_1^0, \Delta H_{ads})$ in the kinetic expressions. Following the initial input of the independent variables, the dependent variables $(P_{CO}, P_{O_2}, P_{CO_2}, P_{H_2}, P_{H_2O})$ were calculated with the 4th order Runge–Kutta method [17]. Data fitting of the calculated dependent variables to experimental data was then carried out to derive corrected values of the independent variables with the Marquardt method [17]. Afterwards, these corrected values were fed to the kinetic expressions for the next iteration. The final values of the dependent variables were reached by minimizing the weighted sum of squared residuals for dependent variables. The above algorithm was realized with MATLAB.

2.3. Quasi-3D non-isothermal reactor model

The first part of the non-isothermal reactor model was the construction of mole balance and energy balance equations. The kinetic rate expressions of different reactant species in Eqs. (10)–(12) were used as the mole balance equations. The pressure drop across the reactor was neglected in the modeling for m-PBR's since the Ergun equation [18] suggested acceptably negligible pressure drop for the flow conditions and reactor characterizations used in the modeling. The first law of thermodynamics was used for the derivation of the energy balance equation (Eq. (13)) [18]. After dissecting the heat flow $(d\vec{Q})$ into radial and axial terms, a partial differential equation (Eq. (14)) is obtained as the energy balance equation in the model. The first bracketed term is the heat removal in axial and radial directions and the second is the heat generation from the three reactions in PrOx:

$$\frac{d\vec{Q}}{dV} - \sum_{i=1}^{5} \left[H_i^\circ(T_R)\frac{dF}{dV} \right] = 0 \tag{13}$$

$$\left\{ k \left(\frac{1}{r}\frac{\partial T}{\partial r} + \frac{\partial^2 T}{\partial r^2} + \frac{\partial^2 T}{\partial l^2} \right) \right\} - \left\{ \sum_{i=1}^{5} \left[H_1^\circ(T_R)\frac{dF_i}{dV} \right] \right\} = 0 \tag{14}$$

The next part describes the quasi-3D structural model of the reactors. Cylindrical geometry was used to approximate both the microchannel and the packed bed. Thus the 3D reactor structure can be represented by the quasi-3D finite difference grid in radial and axial directions, as shown in Fig. 2. The volume of a differential 3D element is therefore calculated as $2\pi[(j-1)\,dr]\,dr\,dl$ (Fig. 2).

As the third step, derivatives were transformed to finite difference forms by a well-established approach [19,20]. The resulting linear equations are shown in the following equa-
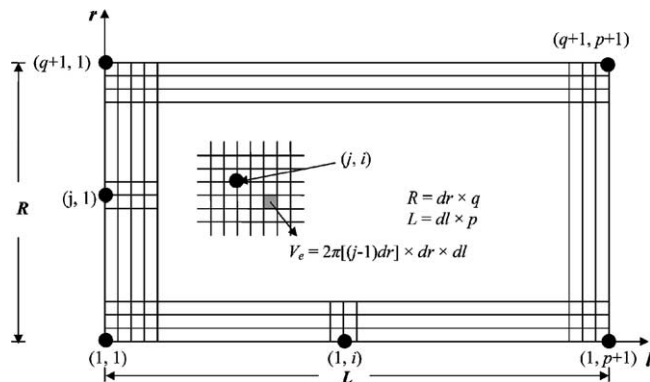

Fig. 2. The finite difference grid in radial (r) and axial (l) directions. Each grid point is denoted as (j,i) with R as the reactor radius and L as the reactor length.

tions:

$$\frac{\partial^2 T_{(j,i)}^{(k+1)}}{\partial r^2} = \frac{1}{(dr)^2}(T_{(j+1,i)}^{(k)} - 2T_{(j,1)}^{(k)} + T_{(j-1,i)}^{(k)}) \tag{15}$$

$$\frac{\partial^2 T_{(j,i)}^{(k+1)}}{\partial l^2} = \frac{1}{(dl)^2}(T_{(j,i+1)}^{(k)} - 2T_{(j,i)}^{(k)} + T_{(j,i-1)}^{(k)}) \tag{16}$$

$$\frac{\partial T_{(j,i)}^{(k+1)}}{\partial r} = \frac{1}{2\,dr}(T_{(j+1,i)}^{(k)} - T_{(j-1,i)}^{(k)}) \tag{17}$$

Finally, the Gauss–Seidel iteration method [20] was used to solve the mole balance and energy balance equations simultaneously. The sum of squared residuals was minimized as the criterion to end iteration.

3. Results and discussion

3.1. Qualitative analysis of heat transport limitations in reactors

Our additional PrOx studies [1] discussed the heat transport resistance with Mear's criterion, which suggested that interparticle heat transport dominates in both the microreactor and m-PBR's compared to intraparticle and interphase heat transport. The Damkőhler number (Da) was then used for qualitative comparison of heat transport limitations for the two types of reactors, in which the heat conduction distance (t_{cat}) is the determining factor. The t_{cat} of the thin-film catalyst (5×10^{-6} m) is orders of magnitude smaller than that for the packed-bed catalyst ($\sim 2 \times 10^{-3}$ m). Due to the quadratic dependence of Da on the t_{cat}, Da of the m-PBR with 2×10^{-3} m radius (2 mm m-PBR) is more than five orders of magnitude of Da for the microreactor. The Mear's criterion then suggested severe heat transport limitations for the m-PBR's for the highly exothermic PrOx reaction.

3.2. Temperature gradients for the microreactor and the 2 mm m-PBR

In this section, in order to derive the correlations between reactor size and reaction performance, we discuss the temperature distribution and PrOx performance for both types of reactor based on identical operating conditions (reactor wall temperature and weight hourly space velocity (WHSV)).

The modeling results of the microreactor showed essentially isothermal temperature distribution in the thin-film catalyst even at the highest operating temperature (300 °C), supporting our qualitative analysis with Mear's criterion. Also as predicted, the results for the 2 mm m-PBR showed significant temperature gradients and effect on PrOx performance, as shown in Figs. 3 and 4. Fig. 3 plots the conversions (O_2, CO, H_2) and selectivity (CO_2) along the reactor length for three representative wall temperatures ($T_w = 120$, 180, 220 °C). Fig. 4 shows the 3D figures of the temperature distribution also at these wall temperatures.

As described in Section 2.3 and Eq. (14), the overall product of the reaction rates of the PrOx reactions (Eqs. (1)–(3)) and their reaction enthalpies determine the local heat generation in the reactor. Since the reaction enthalpies for the exothermic oxidations of CO and H_2 are similar (Eqs. (1) and (2)) and the endothermic r-WGS reaction has reaction enthalpy almost one order of magnitude smaller (Eq. (3)), the amount of local heat generation is controlled by the oxidation reactions and roughly proportional to the local O_2 reaction activity. This argument allows the correlation of the modeling results of reaction and temperature distribution as follows.

Due to the low O_2 reaction activity at $T_w = 120$ °C (Fig. 3a), the temperature gradient is negligible in both axial and radial directions (<1 °C), as shown in Fig. 4a. At 180 °C, O_2 reaction activity is mild up to $l = 2 \times 10^{-2}$ m, which leads to small heat accumulation and temperature gradients in this region. However, the sudden increase of both CO and H_2 oxidation activity between $l = 2 \times 10^{-2}$ to 2.5×10^{-2} m causes a dramatic increase of net O_2 reaction activity, leading to temperatures much higher internally than at the wall (Figs. 3b and 4b). Figs. 3c and 4c show the results of reaction and temperature distribution at $T_w = 220$ °C; more severe temperature gradients are developed close to the entrance of the reactor since full O_2 conversion is reached at a length of only 10^{-3} m.

In order to gain further insight into the effect of wall temperature on hot spot formation, the axial temperature distribution in the center ($r = 0.0$ m) and the radial temperature distribution at $l = l_{T_{max}}$ are plotted in Figs. 5 and 6, respectively. Fig. 5 shows that the temperature gradients become more dramatic and move upstream with higher wall temperatures. With the wall temperature increases, full conversion of O_2 (with CO and H_2) takes place in shorter reactor lengths. Due to the similar reaction heat of CO and H_2 oxidations, the total heat generated by full O_2 conversion is almost constant eve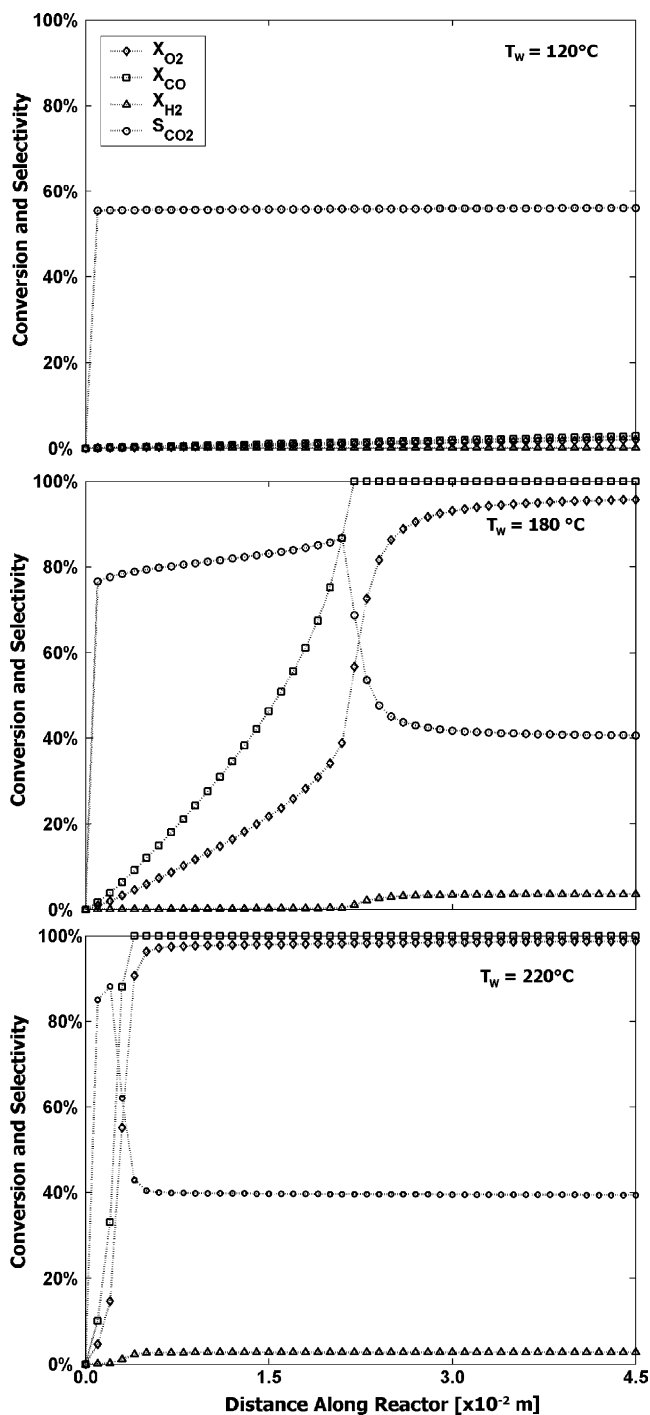n as selectivity varies. A shorter length for full O_2 conversion thus implies a higher density of heat accumulation and consequently larger temperature gradients in the region close to $l_{T_{max}}$. Correspondingly, the radial temperature gradients also increase with the wall temperature, as shown in Fig. 6.
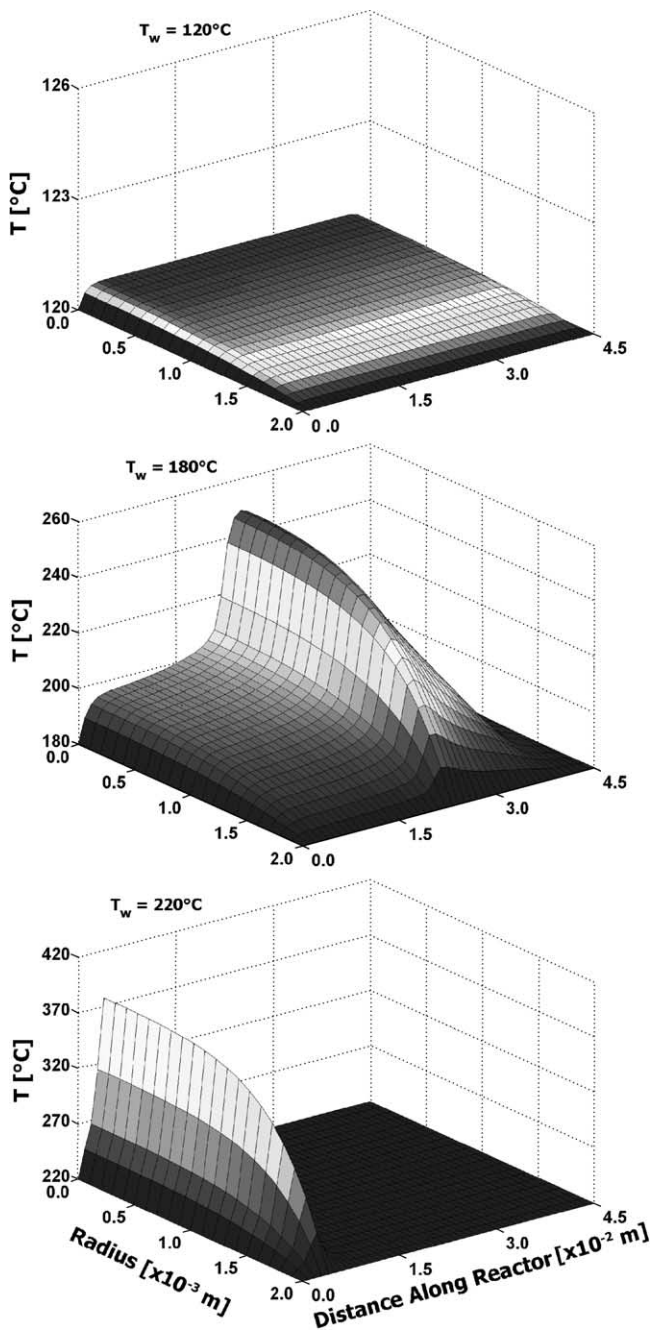

Fig. 3. O_2, CO, H_2 conversion and CO_2 selectivity along the reactor length of 2 mm m-PBR with $T_w = 120$, 180, 220 °C. WHSV = 1500 h^{-1}.

Fig. 4. 3D plots of reactor temperature distribution for the 2 mm m-PBR with $T_w = 120, 180, 220\,°C$. WHSV $= 1500\,h^{-1}$.

3.3. Operating temperature window of PrOx

Fig. 7 plots the modeling results of CO conversion at different wall temperatures for the microreactor and m-PBR's with 2×10^{-3} and 4×10^{-3} m radii (2 and 4 mm m-PBR's), all with the same WHSV ($1500\,h^{-1}$) and isothermal wall temperatures. The CO conversion curve for the microreactor essentially coincides with the result for ideal isothermal operation. On the contrary, the CO light-off curves for the m-PBR's shift to lower temperatures and CO conversion drops significantly at higher wall temperatures. The light-
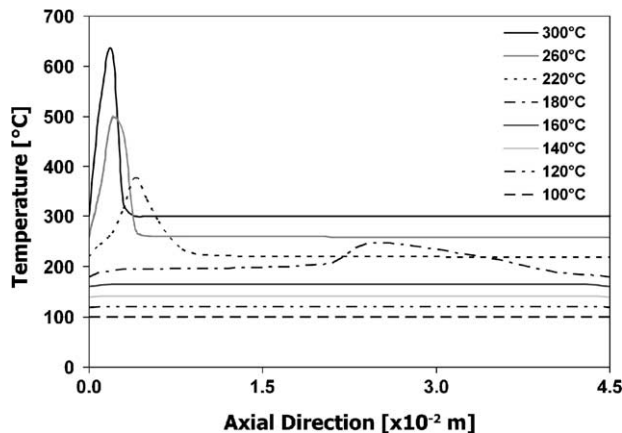

Fig. 5. Temperature distribution in the axial direction at $r = 0.0$ m for the 2 mm m-PBR at different wall temperatures. WHSV: $1500\,h^{-1}$.

off shift to lower temperature is due to an increase in CO oxidation rate at local hot spots. With further temperature increase, however, these temperature non-uniformities activate the r-WGS reaction, leading to a drop of net CO con-
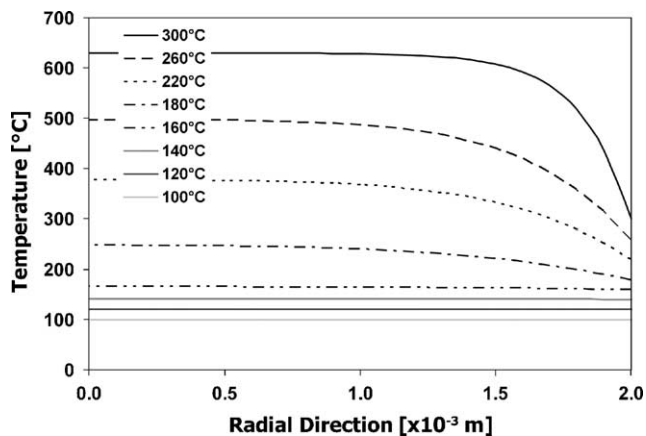

Fig. 6. Temperature distribution in the radial direction at $l = l_{T_{max}}$ for the 2 mm m-PBR at different wall temperatures. WHSV: $1500\,h^{-1}$.
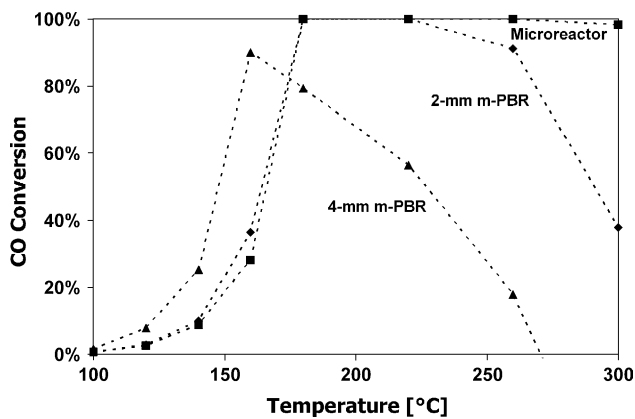

Fig. 7. CO conversion vs. different reactor wall temperatures for the microreactor, 2 and 4 mm m-PBR's. WHSV: $1500\,h^{-1}$.
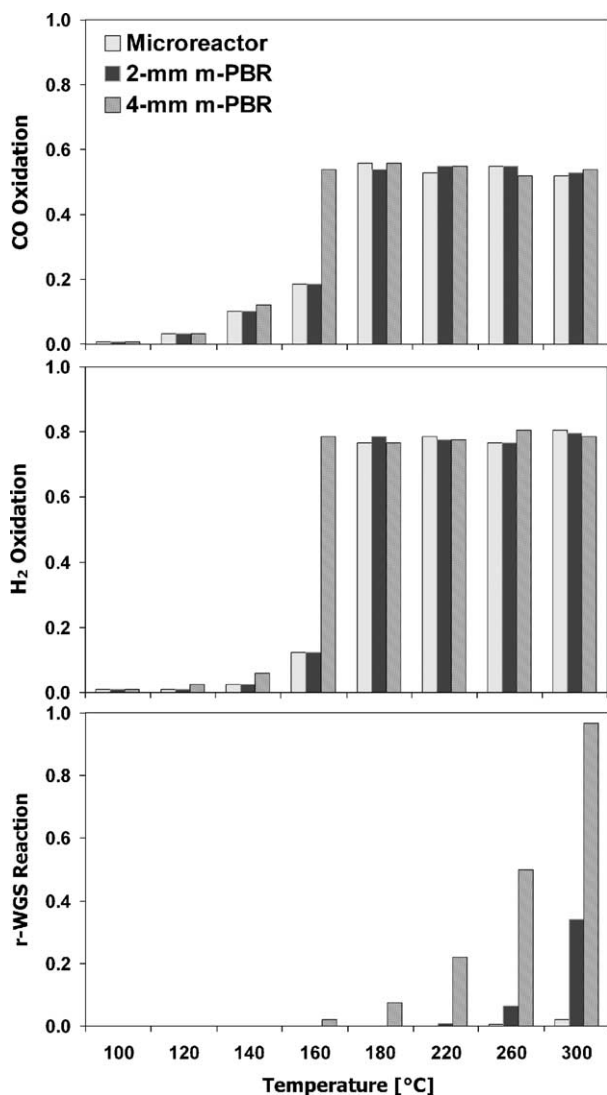
Fig. 8. The average reaction rates for CO oxidation, H_2 oxidation and the r-WGS reaction at $T_w = 120, 180, 220\,°C$ for the microreactor, 2 and 4 mm m-PBR's. All vertical axes have the same scales, with full scale (1.0) corresponding to 3.9 mol/kg s.

version. These phenomena are seen to intensify as the radial thermal resistance increases (4 mm versus 2 mm). The inability of the 4 mm m-PBR to reach 100% conversion is indicative of severe hot spots even at relatively low wall temperatures. The CO conversion curves from literature PrOx studies with m-PBR's [2–4] agree qualitatively with these modeling results and thus can be understood with the above discussion. However, due to the lack of detailed kinetic data of other PrOx catalysts in the literature, further effort to specifically predict PrOx behavior for these PrOx reactors is impractical.

Fig. 8 then shows the average reaction rates of CO oxidation, H_2 oxidation and r-WGS reaction for the microreactor, the 2 and 4 mm m-PBR's at the same reaction conditions used in Fig. 7, which were calculated by integrating and then averaging the reaction rates over the entire reactor volume.

It clearly indicates that the m-PBR's has increasing r-WGS reaction rate with wall temperatures higher than 220 °C. Consequently, these phenomena are more significant for the 4 mm than the 2 mm m-PBR. In contrast, the isothermality within the microreactor effectively minimizes the extent of the r-WGS side reaction at these temperatures.

Additional results from our model also clarified other factors that influence the reactor temperature profile and PrOx reaction performance. For example, perfect wall insulation leading to adiabatic operation results in heat removal only through the axial direction and as expected, eliminates radial temperature gradients. Heat accumulation is more severe than in the isothermal wall condition, leading to an even higher local temperature and adverse PrOx performance. Similarly, a higher catalyst active metal density causes large O_2 conversion in shorter reactor lengths and higher local temperatures. Thus thermal management through the control of reactor radius, heat exchange conditions and catalyst loading density is crucial in the PrOx reactor design.

4. Conclusions

Divergence of the PrOx reaction behavior between a microreactor with thin-film catalyst and m-PBR's were discovered and delineated here. A quasi-3D finite difference non-isothermal reactor model was developed to gain insight into the origins of the differences. The microreactor has negligible temperature gradients within the entire experimental temperature range due to its small t_{cat}. On the contrary, due to its greater effective t_{cat}, the m-PBR's develop significant temperature gradients in both radial and axial directions under the conditions considered here experimentally and through simulation. For wall temperatures before and during light-off, the slight local temperature gradients in the m-PBR's cause the light-off curve to shift to lower temperatures. At moderately higher temperatures, severe temperature gradients rapidly develop in the m-PBR's which degrade the PrOx performance by activating the r-WGS reaction and decreasing the net CO conversion.

References

[1] X. Ouyang, L. Bednarova, P. Ho, R.S. Besser, AIChE J. (2004), in press.
[2] M.J. Kahlich, H.A. Gasteiger, R.J. Behm, J. Catal. 171 (1997) 93–105.
[3] S.H. Oh, R.M. Sinkevitch, J. Catal. 142 (1993) 254–262.
[4] Y. Choi, H.G. Stenger, J. Power Sources 129 (2004) 246–254.
[5] R.H. Venderbosch, W. Prins, W.P.M. van Swaajj, Chem. Eng. Sci. 53 (1998) 3355–3366.
[6] G.W. Roberts, P. Chin, X.L. Sun, J.J. Spivey, Appl. Catal. B: Environ. 46 (2003) 601–611.
[7] H. Surangalikar, X. Ouyang, R.S. Besser, Experimental study of hydrocarbon hydrogenation and dehydrogenation reactions in silicon microfabricated reactors of two different geometries, Chem. Eng. J. 93 (2003) 217–224.

[8] R.S. Besser, W.C. Shin, Deep reactive ion etching characteristics of a micromachined chemical reactor, J. Vac. Sci. Technol. B 21 (2) (2003) 912–915.

[9] S. Zhao, R.S. Besser, Proceedings of the Sixth International Conference on Microreaction Technology, New Orleans, LA, 2002, pp. 289–296.

[10] A. Manasilp, E. Gulari, Appl. Catal. B: Environ. 37 (2002) 17–25.

[11] M.J. Kahlich, H.A. Gasteiger, R.J. Behm, J. Catal. 171 (1997) 93–105.

[12] R.H. Nibbelke, M.A.J. Campman, J.H.B.J. Hoebink, G.B. Marin, J. Catal. 171 (1997) 358–373.

[13] D.H. Kim, M.S. Lim, Appl. Catal. A: Gen. 224 (2002) 27–38.

[14] X. Ouyang, P. Ho, H. Chen, W.C. Shin, L. Bednarova, W. Lee, R.S. Besser, S. Pau, C.S. Pai, J.A. Taylor, W.M. Mansfield, AIChE 2003 Annual Meeting Proceedings, 2003.

[15] Y. Choi, H.G. Stenger, J. Power Sources 124 (2003) 432–439.

[16] J.M. Moe, Design of water-gas shift reactors, Chem. Eng. Process. 58 (1962) 33–36.

[17] A. Constantinides, N. Mostoufi, Numerical Methods for Chemical Engineers with MATLAB Applications, Prentice-Hall, Upper Saddle River, NJ, 1999, pp. 598–728.

[18] Steady state nonisothermal reactor design, in: H.S. Fogler (Ed.), Elements of Chemical Reaction Engineering, 3rd ed., Prentice-Hall, Upper Saddle River, NJ, 2000, pp. 339–425.

[19] Partial differential equations, in: S.C. Chapra, R.P. Canale (Eds.), Numerical Methods for Engineers, 3rd ed., McGraw-Hill, 1998, pp. 812–848.

[20] J.D. Hoffman, Numerical Methods for Engineers and Scientists, Part 3, 2nd ed., McGraw-Hill, 1992.